ADVANCED ENERGY MATERIALS
www.advenergymat.de

An Assessment of Blended Short Loop Recycled Graphite Electrodes Using X-Ray Micro-Computed Tomography

Sean Scott, Wenjia Du, Rosie Horwood, Chunhong Lei, Paul Shearing, and Andrew P. Abbott**

With various battery directives necessitating the composition of recycled electrode materials this study manufactures anodes containing various ratios of pristine and reclaimed graphite from end-of-life (EOL) cells. Two approaches that can be used to delaminate graphite are using ultrasonication (USD) and simple water delamination (WD). X-ray micro-computed tomography is used to characterize the graphite particles and show that particle fracturing is evident with both methods, but key structural metrics such as particle radius and diffusivity varied significantly. It is shown that blending 20% recovers material with 80% pristine graphite causes no statistically significant difference in the performance of the cells. This suggests that recycling anode materials can be achieved without significant post-processing required. For WD anode material, the spherical graphite particles are maintained, whereas USD significantly changes the morphology and produces a large amount of "needle-like" particles. Using 100% reclaimed anode material causes the performance of the cell to decrease to 279 mAh g^{-1} for WD material and 254 mAh g^{-1} for USD graphite. The use of "blended" electrodes using WD graphite and pristine material creates electrodes with a comparable Li^+ flux and electrochemical performance to a pristine graphite reference of 300–315 mAh g^{-1}.

1. Introduction

As electric vehicles (EVs) continue to rapidly gain market share in the transportation sector, with 40 million EVs on the roads as of 2023,[1] an ongoing concern is the implementation of an effective end-of-life (EOL) strategy that can accommodate the broad range of different chemistries and designs of lithium-ion batteries (LIBs).[2,3] Current waste treatment strategies involve the shredding of battery modules to create a mixed black mass, which is subsequently treated with pyrometallurgical and hydrometallurgical processes.[4,5] Most cathode materials are reprocessed by long-loop recycling, returning them first to their precursor salts.[6,7] The same approach is not possible for spent anode materials. New battery legislation such as the European Union battery directive, requires larger percentages of recycled materials in new batteries,[8] although graphite is not included as new reconditioning or direct recycling methods need to be developed.[9–11]

Direct recycling is a process whereby materials are recycled without returning them to the precursor stage, however, this can only be used for relatively pure waste streams with negligible degradation.[9] This can only usually be applied to production scrap, (the dominant source of recycled material until 2030[12]) or from disassembled cells. A recent techno-economic assessment of the disassembly of numerous commercial LIBs concluded that due to the complexity of the battery design, automation would be essential to make dismantling and direct recycling methodologies economically viable due to the extensive time requirements compared to shredding.[10]

Recent studies have identified alternative disassembly and delamination strategies that could circumvent shredding. This study will assess two such processes in regard to the structural changes brought about by the delamination procedure. These processes are similar and have been shown to operate successfully on graphite anodes in a short time span and at room temperature. The first is an ultrasound-based methodology using acoustic pressure within a liquid medium to break the adhesive bonds between the active material and the copper current collector.[13] The second process simply uses water to react with residual

S. Scott, R. Horwood, C. Lei, A. P. Abbott
School of Chemistry
University of Leicester
Leicester, UK
E-mail: sas100@leicester.ac.uk; apa1@leicester.ac.uk

S. Scott, W. Du, C. Lei, P. Shearing, A. P. Abbott
The Faraday Institution
Quad One
Harwell Science and Innovation Campus
Didcot, UK

W. Du, P. Shearing
Department of Engineering Science
University of Oxford
Parks Road, Oxford OX1 3PJ, UK

The ORCID identification number(s) for the author(s) of this article can be found under https://doi.org/10.1002/aenm.202403498

DOI: 10.1002/aenm.202403498

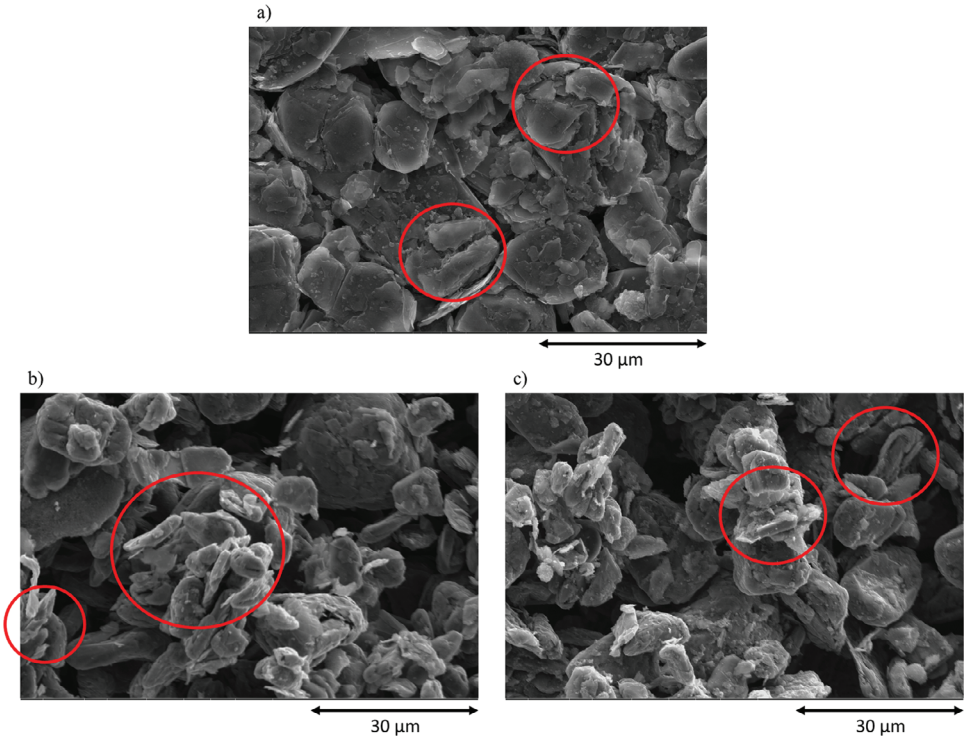

Figure 1. Scanning Electron Microscopy images taken at an excitation voltage of 10kV, at a 5000x magnification showing the condition of the graphitic material a) before delamination b) after ultrasound delamination, and c) after water delamination. Red circles indicate particles that have cracked or fractured.

lithium within the graphite causing delamination.[14] Previously an electrochemical assessment of remanufactured anodes recovered using the ultrasound delamination process has been carried out. Here, anodes made with wholly recovered graphite achieved an initial battery capacity of only 87% of the capacity achieved by pristine materials.[15]

X-ray micro-computed tomography (X-ray micro-CT) is a powerful tool to characterize the internal structure and morphology non-destructively in 3D, accelerating fundamental research across various topics from materials science to medical engineering, geologies, and paleontology.[16] In the last decade, this tool has been successfully applied to electrochemical devices, such as batteries.[17–19] The spatial resolution spans tens of millimeters to tens of nanometers, enabling researchers and engineers to characterize electrode particles and their porosities within small pieces of electrode materials, aiding in understanding the first-life aging and relevant mechanisms of materials failure.[20,21] It can also be used to evaluate newly developed materials or optimize the manufacturing processes.[22,23] A recent study involved the use of this tool to inspect the state of health of large EOL batteries for repurposing and validations.[24] Furthermore, it allows 4D observations (3D plus time), which correlates structural dynamics to the performance and lifetime of batteries.[25] In this study, a series of recovered and remanufactured anode materials are characterized by X-ray micro-CT after a direct recovery methodology is implemented for the first time. Two alternative delamination processes (water-based and ultrasound) are tested to observe the effect they have on the final, remanufactured material. The effect of blending different amounts of recovered material with uncycled graphite is also compared.

2. Results and Discussion

2.1. Scanning Electron Microscopy Imaging

Initially, the anodic materials before and after delamination were imaged using scanning electron microscopy (SEM) to assess the differences brought about by the delamination methodology used, prior to remanufacturing. These images are shown in **Figure 1**. Most of the visual changes before and after delamination, in both cases originate from the fact that before delamination (Figure 1a) the graphite is adhered to the current collector, whereas afterward the majority of the binder has been removed from the material, as seen in Figure S1 (Supporting Information), and the active material is present as a powder. However, there are some indications, highlighted by the red circles in Figure 1, of particle fracturing namely the particle cracking, breakdown of the spherical structure, and the presence of a wide range of particle sizes (≈3–30 µm in diameter). As these morphological features are present before and after delamination, it is assumed that they are a result of degradation during their first life, such as volume expansion or graphite exfoliation, rather than from the delamination method used to recover the active material.[26] However, it should be noted that both methods do rely on the reaction between residual lithium within the graphite and the water-based delamination solutions, with the resulting pressure, potentially causing further particle breakdowns during

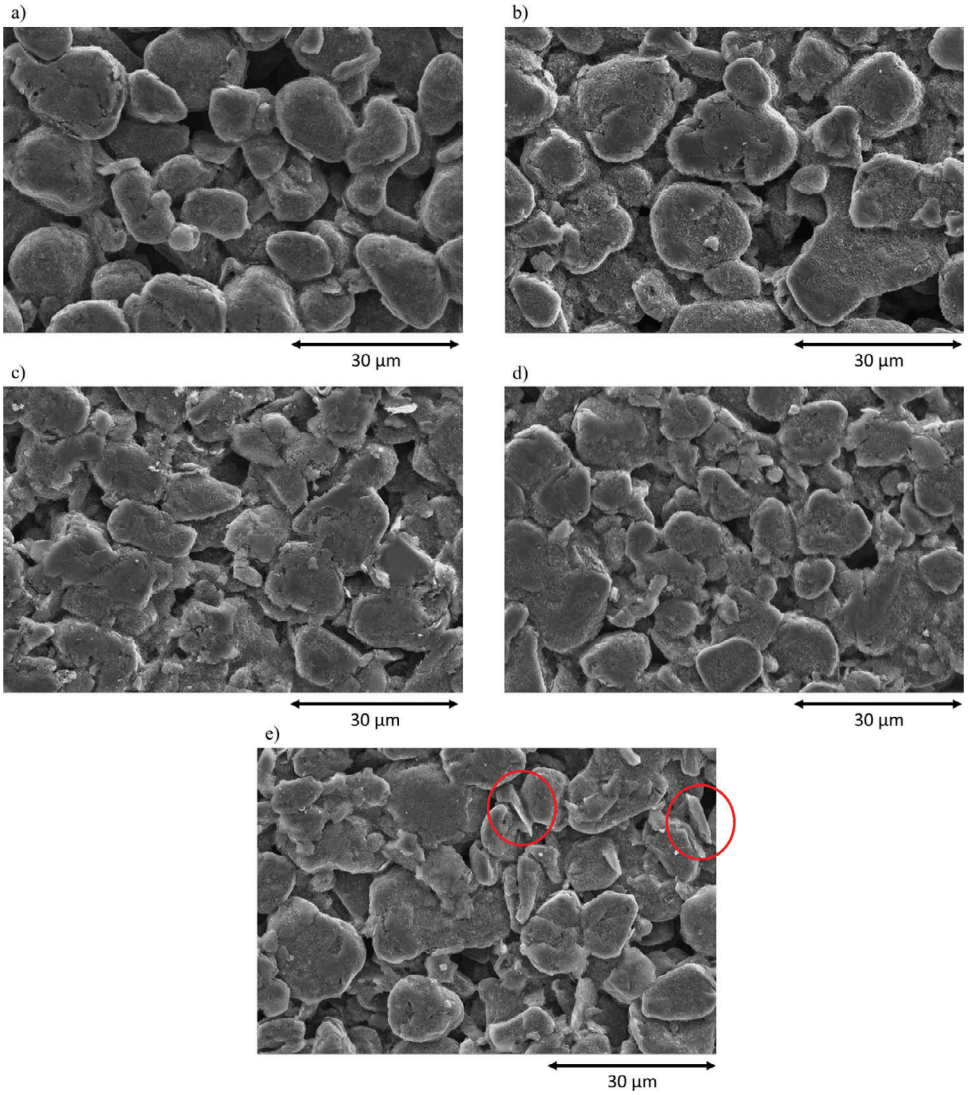

Figure 2. Scanning Electron Microscopy images taken at an excitation voltage of 10 kV, at a 5000x magnification showing the morphology of the graphite anodes when remanufactured using different ratios of pristine graphite and recovered graphite (P:R). a) 80:20 (WD), b) 50:50 (WD), c) 20:80 (WD), d) 0:100 (WD), e) 0:100 (USD).

delamination. Additionally, the use of a ball milling step may also cause damage to the particulate and lead to this particle size range. However, ball milling is a required step in preparing the resulting graphite for remanufacturing and is used for both delamination techniques investigated, any structural differences between samples are therefore predicted to be a result of the delamination step, rather than ball milling.

The formation of these fractured and smaller particles is likely to have an effect on remanufactured anodic properties such as the electrode-specific surface area, which can affect essential processes such as solid electrolyte interface (SEI) formation and could cause increased surface inhomogeneities, which promote localized electrochemistry. Both of these could increase cell resistance and cause accelerated battery aging by facilitating localized structural defects, such as cracking, inducing voltage gradients across the electrodes, and lithium plating.[27–29] Both of these contribute to key battery parameters such as capacity, power density, and the overall stability of the resulting material.[30,31] Therefore, it is essential to assess the structure of these materials after delamination methodologies to ensure no further degradation has occurred and to ensure that batteries made with these reclaimed materials can attain comparable performance to pristine materials. Showcasing the viability of these methods in establishing a circular economy for anodic materials.

Similar images were then taken of the resulting electrodes when remanufactured using different ratios of pristine and recycled graphite. It is important to image the remanufactured electrodes rather than just the intermediate recovered material as the fragmentation of the recycled material can be exacerbated during the mechanical action of electrode production. In these SEM images, shown in **Figure 2**, the morphological differences between EOL and pristine graphite are clearer. Figure 2a–d shows that as the proportion of water delaminated (WD), recycled graphite used in the anode active material increases, there are minimal

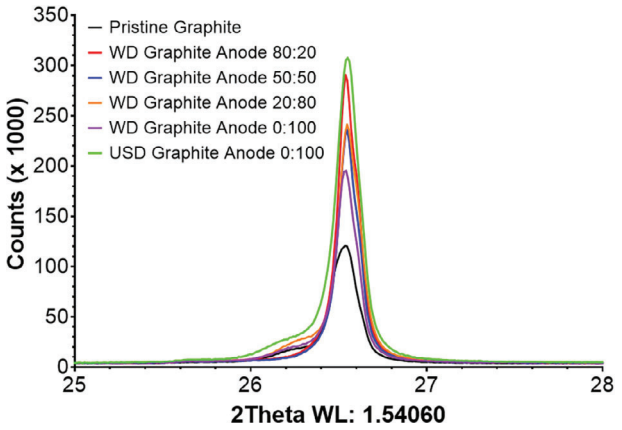

Figure 3. X-ray diffraction curve relating to the peak assigned to the graphite crystal structure of P 63 m c measured at ≈26.55°. The associated peak area data to this curve is given in Table 1. (WD = water delaminated, USD = ultrasound delaminated). The curves have been aligned relative to the peaks associated with the copper current collector.

changes within the anode material morphology, in terms of the overall appearance of the graphitic particles. However, there does seem to be a greater amount of the smaller, <3 µm, graphite particles present. Meanwhile, Figure 2d,e show that, while both electrodes have significant particle fracturing, the ultrasound-delaminated (USD) material indicates further degradation of the graphitic structure. Here, some particles that are no longer spherical, instead showing needle-like structures as highlighted by the red circles. Therefore, while the use of recycled graphite presents some structural defects that could lead to issues during the formation and use of the cells, the use of the ultrasonic delamination methodology on graphite anodes causes further, significant damage to the structure of the active material. The use of ultrasound during delamination is unraveling the spherical graphite particles, creating regions of the anode with the graphite that resembles the flaked nature of natural graphite. This could further exacerbate the previously discussed issues with using EOL graphite, namely changes in specific surface area and surface inhomogeneities, leading to a localization of the electrochemistry during cycling and the formation of an inconsistent SEI layer, inducing increased electrolyte decomposition and decreased anodic stability.[27,28] Further 3D characterization of these materials is essential, such as the application of X-ray micro-CT to determine whether the 2D observations here are representative of the entire anodic structure and to determine any effects the use of recycled materials, or delamination technique has on the crystal structure, characterize the knock-on impact this has on cell performance, and benchmark the data for future validations.

2.2. X-Ray Diffraction Analysis

To ensure that no significant crystal structure changes occurred as a result of the delamination procedures, X-ray diffraction (XRD) was carried out on each electrode. This data is highlighted in **Figure 3** and **Table 1**. As may be expected, this data does not show any significant changes to the position of the XRD peak with all samples having a peak maxima position of ≈26.54°–26.55°, which is consistent with other graphite materials.[32,33]

Table 1. X-ray diffraction calculated peak maximum, peak area, and peak width, via the full-width half maximum (FWHM) and crystallite size data for the diffraction pattern shown in Figure 3, across the range of 26.3° and 26.9°.

Pristine: Reclaimed Graphite Ratio	Peak Maxima [°]	Peak Area	Peak width, FWHM [°]	Crystallite Size [Å]
Pristine Graphite	26.544	21.00	0.125	678.6
80:20 (WD)	26.544	35.09	0.125	680.6
50:50 (WD)	26.548	28.49	0.126	668.5
20:80 (WD)	26.553	28.11	0.130	629.2
0:100 (WD)	26.539	23.94	0.132	634.0
0:100 (USD)	26.550	38.66	0.138	581.2

This shows that no crystal structure changes are present regardless of the amount of recycled graphite used in electrode formulation. Table 1 also shows multiple parameters obtained from the peaks outlined in Figure 3, peak area and peak width, using full-width half maximum (FWHM) and crystallite size to qualitatively show how the structural defects that may be present within the recycled graphite affect the resulting anode materials. This can be achieved as these metrics correlate to the number of diffracting species present within the sample and the crystallite size/homogeneity of the diffracting species, respectively.

For the samples analyzed in this study, the peak area and the peak width both increase when recycled graphite content is introduced. This indicates that when EOL graphite is used in anode materials a greater number of diffracting species are present which contribute to a larger XRD peak intensity/area, and these species are generally smaller, leading to a broadening of the XRD diffraction pattern resulting in a larger FWHM and peak area correlating to a lower crystallite size.[34] While this result is consistent with the SEM images shown in Figure 2, which showed particle fracturing when more EOL graphite was used as the active material, as the pristine and recycled graphite come from different original sources this could also be partially responsible for the FWHM value differences. It should also be noted that peak broadening could also be a result of other inhomogeneities present within the recycled graphite material, such as graphite lattice defects, brought about by aging during the first use, and the orientation of the fractured graphitic layers. This could explain why the ultrasound delaminated graphite sample possesses the largest peak area and width, due to the larger degree of fracturing and particle deformation seen in the SEM imaging. In order to confirm and fully evaluate the extent of the graphite fragmentation and the effect this could have on lithiation, X-ray micro-CT and electrochemical characterization was necessary.

2.3. X-Ray Micro-Computed Tomography

3D microstructures of different graphite samples characterized by X-ray micro-CT are presented in **Figure 4**. A region of interest (ROI) of 130 × 300 × 300 pixels (ca. 30 µm × 69 µm × 76 µm) was cropped from the entire sample to show the local morphologies. Similarly, to the previous SEM images, the pristine graphite (Figure 4a,e) shows an intact structure with "droplet or round" shape and has the least local defects within each particle.

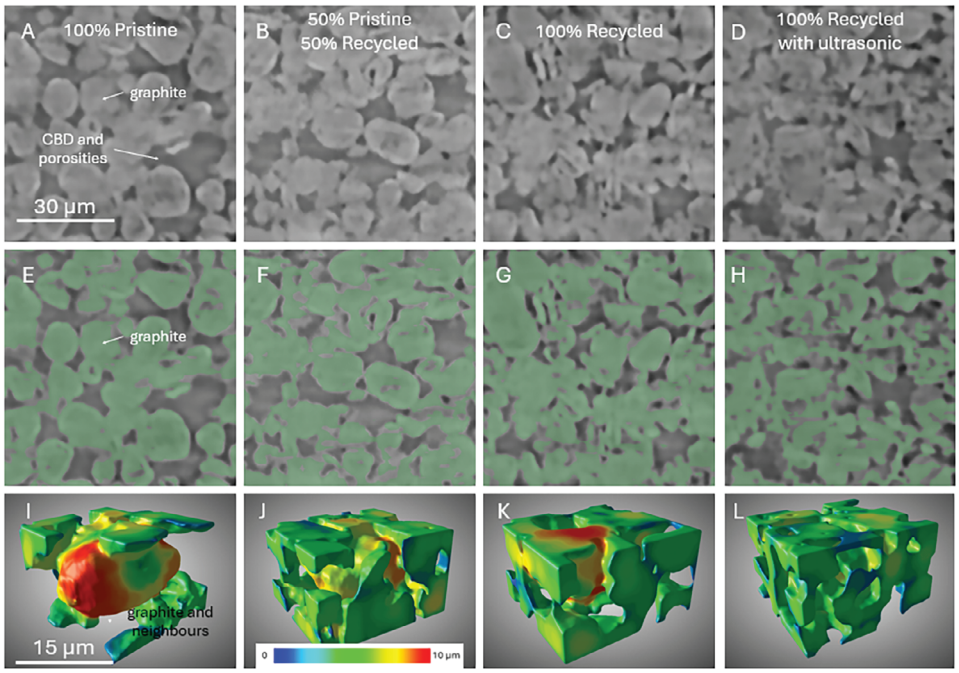

Figure 4. X-ray tomographic imaging of the graphite anode materials, showing the 2D raw (1st row) and AI-segmented (2nd row) microstructures and morphology of the graphite anodes when remanufactured using different ratios of pristine graphite (1st column) and recovered graphite (P:R) 50:50 (WD) (2nd column), 0:100 (WD) (3rd column), 0:100 (USD) (4th column). 3D microstructure of an individual graphite with neighbors and channels (3rd row).

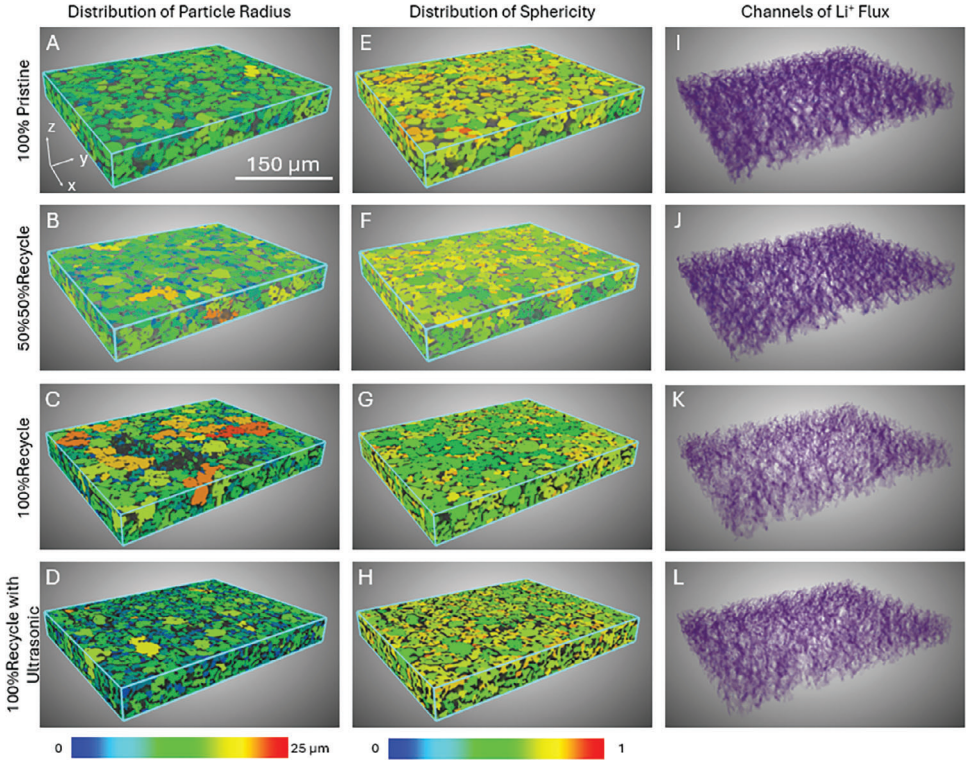

Figure 5. 3D visualizations of particle radius (1st column) and sphericity (2nd column) of graphites, as well as their Li^+ ion flux simulated on the 3D channels of porosity (3rd column) for different ratios of pristine graphite (1st row) and recovered graphite (P:R) 50:50 (WD) (2nd row), 0:100 (WD) (3rd row), and 0:100 (USD) (4th row).

An example particle of ≈10 µm in size, showing this structure, was extracted from the ROI and rendered in 3D, shown in Figure 4i. Whilst all recycled samples show different levels of structural deficiencies due to electrochemical degradation and/or mechanical influences, it is clear that the method of delamination also contributes to these deficiencies. In Figure 4d,h, it is found that the 0:100 (USD) exhibits the most defective structures with significant numbers of fractures. These fractures show a "needle-like" shape in 2D and a "plate-like" shape in 3D which is likely attributed to the cavitation of the spherical graphite, creating graphite "flakes" throughout the electrode structure. Additionally, water delamination still has an effect on the number of structural defects present within the anodic material, with several of the "needle-like" shapes being observed in Figure 4c,g. However, it is not surprising to observe that the 100% recycled sample has more defective morphologies than in the 50:50 (pristine: recycled graphite) sample. It is clear from these images that the spherical particles have been fragmented, which could allow for the formation of new microscale channels that can benefit ion transportation but could lead to other negative effects such as accelerated electrolyte decomposition and excessive SEI formation.

To further examine the effect of water delamination and ultrasound delamination on graphite morphologies and the effect it could have on subsequent electrochemical performance, an array of quantifications is implemented to extract some key metrics, including graphite particle radius (r), sphericity, phase volume fraction (Vf), specific surface area (Sv) and tortuosity (σ). 3D visualizations of distributions of particle radius (the 1st column) and the associated sphericity (the 2nd column) across four distinct samples are presented in **Figure 5**. Additionally, graphical representations of the aforementioned metrics for each sample

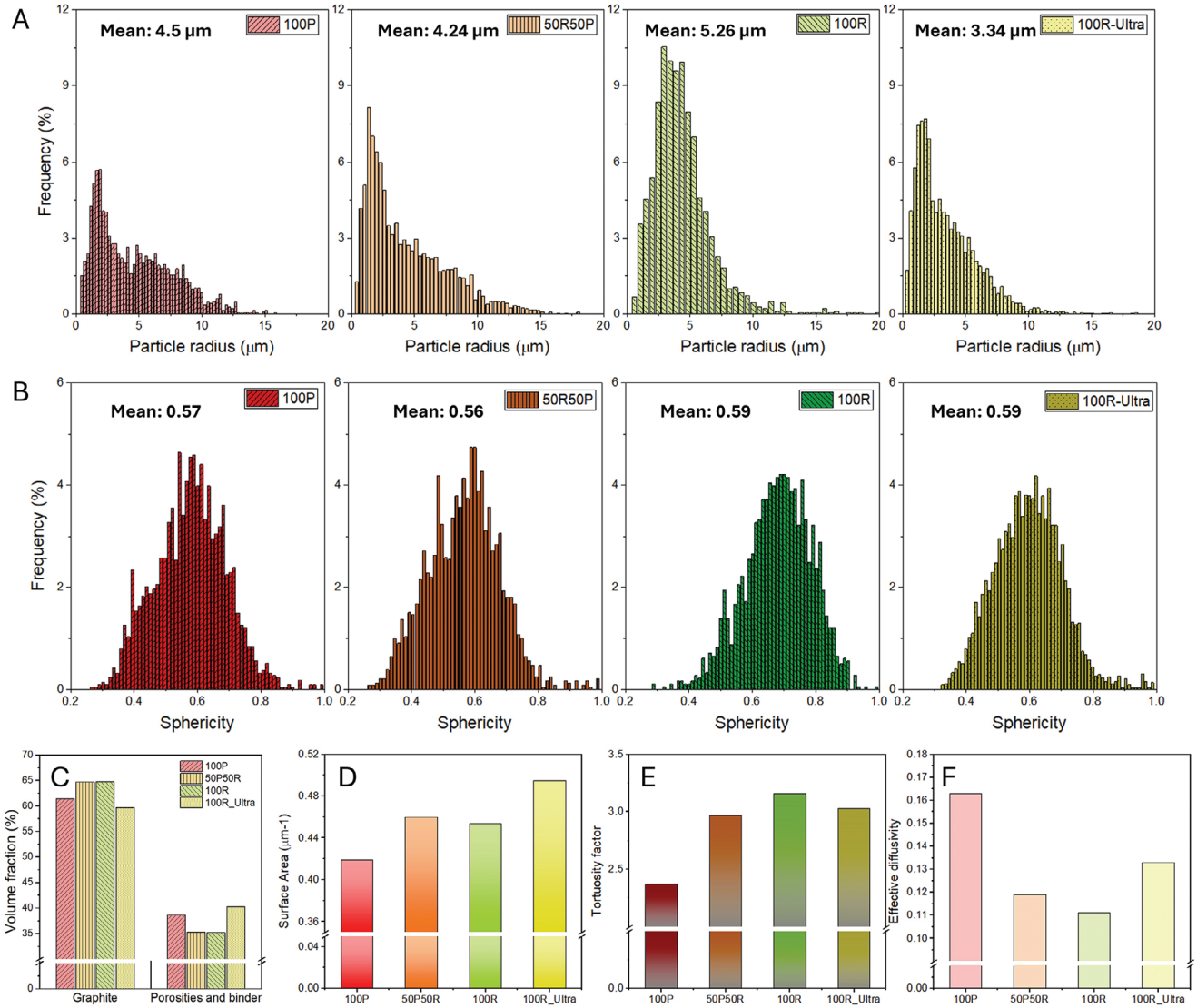

Figure 6. Quantification of the associated graphite anode and porosity. Particle distributions of graphite radius (1st row) and their sphericity (2nd row). (c) Volume fractions, (D) specific surface area of graphite, (E) the tortuosity factor of four different graphite samples with their (F) effective diffusivity for macro-pores and carbon-binder domain (CBD).

are given in **Figure 6**. Overall, the water delamination appears to exert a negligible effect on sphericity, as the values lie in a range between 0.4 and 0.8 (Figure 5e–h).

The pristine sample has a relatively uniform size of graphite as shown in Figure 5a. In contrast, the particle sizes of the anodes using water delaminated graphite were increased, due to recycled particles generally being larger from the repeated intercalation processes across their first usage phase. This change is illustrated by a color transition in the 3D renderings from green/blue to yellow/red, as observed across Figure 5a–c, with the average radius value increasing from 4.5 to 5.26 µm, as seen in Figure 6a. Notably, the sample that used ultrasound delamination saw a significant reduction in the particle size, with an average radius of 3.34 µm (Figure 5d and 6a), which is attributed to fragmentation caused by ultrasonic cavitation of the graphite particles.

Figure 5 illustrates the simulated Li^+ flux based on the 3D microstructure of the carbon-binder domain (CBD) and porosities in both pristine and three recycled states. The sequence of flux mapping is as follows: pristine > 50:50 (WD) > 0:100 (USD) > 0:100 (WD). The comparative results indicate that there are substantial declines in connectivity of Li^+ flux within the samples using recycled graphite, likely resulting from the interior defects within the graphite, such as the "needle-like" particle formation and the volume expansion of the remaining spherical particles. Figure 6 shows how calculated metrics from this technique vary based on the samples analyzed.

2.4. Electrochemical Characterization

Following the structural characterization of the remanufactured graphite anodes, they were incorporated into coin half cells in order to assess their electrochemical performance and how they changes with recycled graphite content. Initially, the cells all underwent formation cycles at 0.1C, the resulting capacity and coulombic efficiency values are detailed in **Table 2**. Voltage profiles for each sample over these initial formation cycles are also given in Figure S4 (Supporting Information). First, the coulombic efficiency data from all the samples show evidence that the SEI layer has formed, which is essential for the long-term stability of the anodic material during cycling.[30] This was seen by the increase in efficiency from <90% in cycle 1 to >98% in cycle 10. It is interesting to note that the coulombic efficiency for the cells using an increasing amount of water delaminated graphite (pristine → 0:100 (WD)) decreases. This seems to correlate with the simulated Li^+ flux assessment made in the previous section, where the 0:100 (WD) sample was the lowest. Although we deduce that the poorer efficiencies may instead be a result of multiple effects, including poorer Li^+ flux and the formation of an unstable SEI. This means that more lithium is consumed and "trapped" within the cell after the first cycle, reducing the efficiency of the cell. While this is mostly rectified in cycle 10, the efficiency values are still somewhat lower the more recycled material is used. The ultrasonically delaminated graphite also possesses a minimized coulombic efficiency on the 10th cycle, which could also be attributed to the relatively low Li^+ flux described in the tomography data leading to a slightly larger irreversible capacity loss.

The incorporation of water delaminated graphite into blended graphite anodes does lead to a drop in capacity performance, which is most notable in the 80:20 (WD) and 50:50 (WD) samples. For these samples, the addition of more water delaminated graphite causes a 5% drop in capacity retention, relative to the pristine graphite cell (330 mAh g^{-1} → 314 mAh g^{-1} → 299 mAh g^{-1}). However, the 20:80 (WD) sample does not follow this trend and seems to retain a similar capacity to that of the 50:50 (WD) sample, whereas solely using graphite that has been recovered via water delamination does lead to further loss in performance. This data implies that the use of relatively small amounts of pristine graphite can supplement electrochemical performance, increasing specific capacities by ≈50 mAh g^{-1} in this instance, but much larger quantities, >80% pristine graphite, are required to achieve capacities expected of typical graphite electrodes. But this data highlights that similar performance can be achieved through the use of smaller amounts of pristine graphite in future electrode materials, minimizing the cost incurred by obtaining and processing new graphite for

Table 2. Formation cycling data for the anodic half-cells investigated in this study. WD = water delaminated recycled graphite used, USD = ultrasound delaminated graphite used. Charge and discharge capacities were obtained by taking an average over multiple coin cells, the standard deviation is given in brackets. "Charge" refers to the movement of lithium into the graphite.

Pristine: Reclaimed Graphite Ratio	Cycle Number	Average Charge Capacity [mAh g^{-1}]	Average Discharge Capacity [mAh g^{-1}]	Average Coulombic Efficiency [%]
Pristine	1	256 (*8*)	227 (*15*)	86.6 (*1.9*)
	10	330 (8)	322 (*13*)	99.6 (*0.1*)
80:20 (WD)	1	272 (*12*)	235 (*9*)	85.1 (*2.6*)
	10	314 (*2*)	312 (*2*)	99.3 (*0.3*)
50:50 (WD)	1	249 (*6*)	215 (*13*)	84.0 (*3.8*)
	10	299 (*6*)	297 (*8*)	99.5 (*0.2*)
20:80	1	251 (*8*)	216 (*7*)	84.0 (*4.7*)
	10	300 (*7*)	289 (*14*)	98.9 (*0.5*)
0:100 (WD)	1	194 (*12*)	157 (*10*)	81.0 (*1.2*)
(WD)	10	254 (*8*)	247 (*4*)	98.4 (*0.3*)
0:100 (USD)	1	259 (*14*)	223 (*19*)	85.1 (*4.0*)
	10	279 (*18*)	270 (*13*)	98.4 (*0.8*)

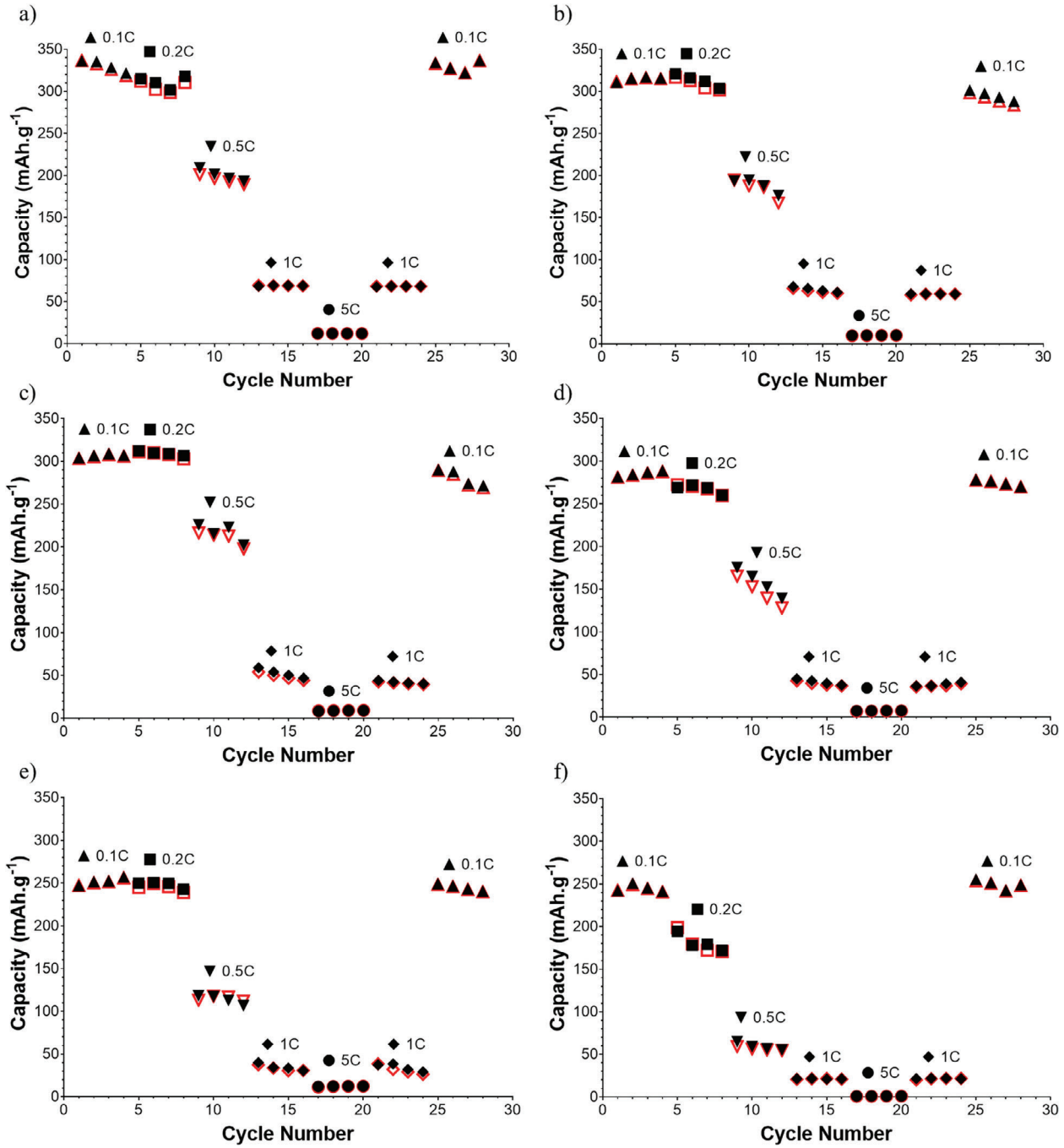

Figure 7. Waterfall plots showing the rate capabilities of the graphite anodes manufactured using recycled graphite at different pristine:recycled graphite ratios. Black symbols show graphite charging, and red outlines show graphite discharging. WD = recycled graphite is water delaminated, USD = ultrasound delaminated. a) Pristine graphite, b) 80:20 WD, c) 50:50 WD, d) 20:80 WD, e) 0:100 WD, f) 0:100 USD. Figure S5 (Supporting Information) shows this data summarized in a single waterfall plot.

battery materials.[35] While the performance shown in the formation cycles closely matches the performances predicted by tomography data for the water delaminated samples, it should be noted that further investigations, such as *in-operando* X-ray techniques, will be necessary to identify potential mechanisms that course the improvements to capacity with relatively small additions of pristine graphite.

Additionally, the rate test data, shown in **Figure 7**, seems to also show good agreement with the tomography data, where the rate capability of the blended material is generally reduced as more water delaminated graphite is incorporated. However, it should be noted that up to the 50:50 (WD) sample, this difference is minimal and shows comparable performance to the pristine material. Furthermore, the blended material exhibits clear improvements

to rate capability and performance relative to the 0:100 (WD) sample, where the capacity at 0.5C was reduced from between 150 and 250 mAh g^{-1}, for the pristine and blended electrodes, to ≈115 mAh g^{-1} for 0:100 (WD). Graphite is already known to possess a poor rate capability at higher current rates due to a variety of phenomena, typically focusing on limited desolvation and diffusivity of lithium during rate-determining lithiation steps.[36,37] This is also indicated by the previous X-ray micro-CT data in Figure 6e,f, where a lower diffusivity causing a poorer Li^+ flux for 0:100 (WD) is observed due to it possessing the largest tortuosity value, which suggests lithium-ion movement has the longest distance among all cases, resulting in the lower capacities and rate performance. In the case of the water delaminated material, it is indicated that the addition of a relatively small quantity of pristine material can allow for comparable cell performance to new graphite electrodes. However, *in-operando* testing should be carried out in the future to analyze the degradation rates of the anode materials, to ensure that localization of electrochemistry within the pristine graphite regions is not occurring.

Comparing the electrochemical performance of the anodes remanufactured from ultrasonically delaminated graphite also shows good agreement with the tomography data. For instance, while the 0:100 (USD) sample possesses a reduced capacity compared to the pristine and blended materials, it has higher capacity retention than the 0:100 (WD) material on the 10th formation cycle, 85% versus 77% respectively. This pattern mirrors that of the simulated Li^+ flux data and is likely a function of the "needle-like" graphite particles having a greater degree of exposed graphitic edge planes, providing greater diffusivity, compared to the water delaminated particles. The ultrasonic cavitation can fragment graphite particles and potentially lead to an increased specific surface area (Figure 6d) and create "new" porosity channels for transportation, which results in an improved ion flux. However, when the rate test data is considered, the ultrasonically delaminated materials have a much poorer rate capability than the other cells. This material seems to have an even greater capacity drop off at 0.5C, leading to an achievable capacity half that of the 0:100 (WD) sample at ≈50–65 mAh g^{-1} compared to 110–115 mAh g^{-1}.

Part of the capacity decrease in Table 2 can be ascribed to structural changes in the graphite particles although some of this can be restored using a variety of regeneration techniques. The mechanism behind the regeneration process is not fully understood although the different techniques as well as other applications for spent graphite have recently been reviewed by Niu et al.[38]

This is consistent with previous studies that carried out electrochemical testing on similar systems, noting a reduced rate capability and when cycled further at low current rates after rate testing, a significant drop in capacity. It is thought that this capacity fade could be a result of the increased specific surface area, observed in Figure 6d, which could enhance the rate of SEI growth and begin to limit the desolvation of lithium ions into the graphite matrix. Meaning that regardless of the improved Li^+ flux within the bulk graphite anode, the capacity at higher current rates is limited by the initial ion transfer across the SEI layer. Additionally, a greater amount of exposed graphite edge planes could facilitate further graphite exfoliation, which could lead to further degradation of the active material. Electrochemical impedance spectroscopy was carried out periodically during testing in order to identify impedance changes that may be causing the specific capacity behavior seen in this work. However, no discernible trends or features were observed. This work is shown in the supporting information in Figure S7 and Table S2 (Supporting Information). Future work in this area could involve in situ/*in-operando* X-ray tomography during extensive cycling to chart how flux changes for all the recycled samples to further confirm the effects that impact the performance of the remanufactured cells, as well as alternative 3–electrode cell setups to further explore the capacity improvements observed when more pristine graphite is added to the recovered electrode materials.[39]

3. Conclusion

Overall, this study has worked to outline how the use of delamination as a separation procedure in the direct recycling of lithium-ion batteries can have a significant impact on the resulting structure and performance of recycled cells. X-ray micro-CT and machine learning-assisted data segmentation have proven instrumental in providing further insight into structural changes of the graphite when two delamination techniques are used: a low-energy, water delamination process and another using high-powered ultrasound to assist delamination. The metrics calculated using this technique allowed for the identification of metrics that may be responsible for the electrochemical performance of recycled materials shown in Section 2.4. For instance, the smaller particle sizes and higher surface area of USD graphite. This was predicted to improve initial capacity versus WD graphite but could lead to enhanced SEI formation over numerous cycles. The determination of the tortuosity indicated that the ion transport of recycled materials could be improved by blending the recycled and pristine graphite together.

The electrochemical characterization of the samples largely confirmed the predicted behavior. During the formation cycles, the 0:100 (USD) cell retained 86% of the capacity of pristine graphite, compared to the 77% retention observed for the 0:100 (WD) graphite. However, upon rate testing the ultrasound material showed a decreased capacity at 0.5C of ≈55 mAh g^{-1} compared to ≈115 mAh g^{-1} for water delaminated graphite. This indicated that despite the initial electrochemical benefits, water delaminated materials would be better suited to creating remanufactured cells, largely due to the retention of the spherical graphite structure. However, it should be noted that due to the significantly lower capacities of materials produced from these recycling methodologies, remanufacturing graphite solely recovered from these processes would not be appropriate. Therefore, blends of pristine and recycled graphite, recovered via water delamination, were investigated to see whether blended anodes may make up for the lower performance of electrodes created solely using recycled materials. The data collected showed the blended materials to be a good "midway point" between the pristine graphite and the 0:100 (WD) material, with the electrochemistry data showing relatively small reductions in capacity up to the 50:50 (WD) sample. Therefore, this work proposes that in order for remanufactured cells to maintain comparable performance to virgin graphite material, while minimizing cost and reliance on the synthesis of "new" graphite, blends of pristine

graphite and recycled graphite, from processes that retain the graphitic structure, may be used.

A follow-up to this work would include using the same techniques to characterize cathode materials that have undergone direct recycling and relithiation processes to ensure that any structural changes these processes incur are accounted for. Especially with cathodes generally requiring harsher conditions to delaminate in direct recycling methodologies due to the binders present, usually polyvinylidene fluoride.

4. Experimental Section

Materials: This investigation used commercial EOL graphitic electrode materials from an anonymous commercial source. The EOL battery was supplied by this source and external project partners were responsible for disassembling the battery and removing the electrolyte from the cells leaving the separated graphite electrode sheets for delamination.

Delamination and Recovery of Materials: The electrode materials were delaminated using two main methodologies, to show the structural impact on the resulting active material. The first method involved the use of an ultrasound delamination method, an original, novel ultrasound unit was used in this study. The unit was equipped with a sonotrode with front face dimensions of 1.5 cm × 21 cm, operating at 20 kHz with a maximum power of 2200 W. A sonication bath is placed underneath the sonotrode, filled with deionized (DI) water and a sample tray to contain the electrode when in use. During the delamination process, the electrodes were fed into the gap between the sonotrode and sample tray, the electrodes were delaminated, and the resulting current collector foil was then fed out of the unit, leaving the active material suspended in the water. This was then filtered using vacuum filtration and more DI water.[13]

The second WD method, as detailed by Sargent et al., submerged electrode sheets in 450 mL of DI water.[14] The resulting active material was retrieved and washed with additional DI water before drying.

Electrode materials from both methods were dried and annealed in air at 500 °C within a furnace (Lenton) to remove polymeric residues as well as any remaining SEI decomposition products that might be present on the graphite particles. Once dried these materials were then ground into a powder using a ball mill (Retsch PM400) equipped with 30 mm agate balls set at 200 rpm for 20 min.

Preparation of Electrodes Via Slurry Mixing: Following delamination, the recovered active material obtained from EOL electrodes was remanufactured via a conventional slurry casting methodology. The slurries were made up with a weight percentage ratio of 90:5:5 active material: conducting additive: binder respectively. All materials manufactured used a carbon black super P (Thermofisher Scientific, >99%) conducting additive and a carboxymethyl cellulose (CMC)/styrene butadiene rubber (SBR) (BDH Chemicals, >99%) binder, where, CMC/SBR was made up using a 1:1 mass ratio. The active material portions of the slurries were varied to assess the effect blending pristine and recycled graphite, which was acquired by water delamination, had on the structure and performance of the cells. The blended electrodes were denoted based on the ratio of pristine: recovered graphite used as the active material. These were 100:0, 80:20, 50:50, 20:80, and 0:100, and then an additional sample where ultrasonic delamination was used to acquire the graphite. In all instances, the mass loadings of the anodes were between 5 and 7 mg cm^{-2}.

During slurry making, the binder solution was made first, combining the CMC/SBR with DI water using a hotplate stirrer. This binder system was then mixed with the carbon black in a THINKY mixer (ARE-250, Intertronics) at 500 rpm for 1 min followed by 2000 rpm for 5 min. This mixing step was then repeated after adding the active material, albeit with an added degassing step at the end set at 2200 rpm for 3 min. After the slurry was formulated, it was cast onto 25 µm thick copper foil with a tape casting coater (MTI corporation, MSK-AFA-1) equipped with a doctor blade set at a thickness of 100 µm and a rate of 7 mm s^{-1}. The electrodes were then left to dry in a fanless Genlab Classic oven (MIINO/50) set at 60 °C until dried. Once dried the cathodes were calendered to a thickness that yielded a porosity of 40% using a hot rolling press (MTI corporation MSK-HRP-1A) set at 6 rpm and 40 °C.

X-Ray Micro-Computed Tomography and Images Analysis: A lab-based X-ray micro-CT instrument (ZEISS Xradia 620 Versa, Carl Zeiss Inc.) was used to characterize the internal morphologies of samples. A 40× lens and a 2048 × 2048 CCD camera detector (bin 1) were used to achieve a voxel resolution at 230 nm with a field of view (ca. 470 µm × 470 µm). A polychromatic cone-beam source using a tungsten target with a voltage set at 100 kV was used. An optimized distance between source-to-sample and source-to-detector was used to achieve the phase contrast to the X-ray image of the electrode materials. For each set of tomographic data, 1601 projections were obtained with an exposure time of 30 s. X-ray projections were reconstructed using a filtered-back projection algorithm (XMReconstructor, Carl Zeiss Inc.). The reconstructed 16-bit datasets (image sequences) were initially imported into Avizo 2022.1 (ThermoFisher Scientific) and then cropped to highlight the regions of interest (35 µm × 230 µm × 300 µm). 3D U-net deep learning (DL) module in Dragonfly (ORS) was used to train a 3D model for pristine anode materials to identify and classify the graphites (green), and carbon-binder domain (CBD) and porosities (pink) based on the grayscale, feature shape, and orientation. Four ground-truth frames at multiple local regions (either close to the current collector or separator or in the middle) were manually segmented to train the 3D model. The computational segmentation is shown in Figure S3 (Supporting Information). The profile of the DL training procedure, including the epochs against the loss function, was also presented. The trained model was then employed to automatically segment raw image sequences. Afterward, quantification Taufactor, an open-source software, was used to extract the electrode metrics, tortuosity factor, and effective diffusivity from the computed tomography image.[40]

Additional Characterization: Analysis of the materials before and after remanufacturing was carried out using multiple techniques in addition to micro-computed tomography. This included SEM, carried out using a FEI Quanta 650 FEG-SEM in secondary electron mode, with an Everhart Thornley detector at a 10 kV excitation voltage at 5000x magnification. energy dispersive X-ray (EDX) measurements were also taken across the same area as the SEM images, over a 10-min period. The elemental mapping of the surface was carried out and calculated by using Aztec EDX software.

XRD was carried out using a powder diffractometer (Bruker D8 Advance), using Cu-Kα radiation ($\lambda = 1.5406$Å). A scanning range of 15°–70° with a step size of 0.01° was utilized for all experiments.

Thermal analysis was utilized before and after the recovery processes to confirm the removal of the binder (data shown in Supporting Information) as well as to confirm a negligible change to thermal stability when using pristine and recovered active materials. This was done primarily via thermogravimetric analysis (TGA) across a heating range of 25–500 °C with a heating rate of 5 K min^{-1}, using a Mettler Toledo TGA/DSC1 with analysis carried out on the associated STARe software (version 12.1). It should be noted that differential scanning calorimetry (DSC) data was also collected but due to the relatively small binder content and the relatively high heat capacity of the copper and graphite, no useful data could be obtained.

Coin Cell Manufacturing and Cycling Methods: The electrochemical performance of the electrodes was also assessed through coin cell cycling. To prepare the electrodes for the coin cells, an electrode press (MTI Corporation, MSK-T-06) was used to cut out 15 mm diameter discs. These were weighed and transferred to a vacuum oven (Binder, VD056-230 V) overnight at 60 °C, before being moved into a glovebox (MBraun, Workstation UNIlab plus/pro – sp/dp). Coin half-cells were then constructed using CR2032 caps and lids, two spacers (1 mm and 0.5 mm width, 16 mm diameter) a wavewasher (15 mm diameter, 1.4 mm width), a separator between the two electrodes (Cellguard, 19 mm diameter) soaked with 40 µL of Li57 electrolyte (Sigma–Aldrich, 1 M $LiPF_6$, ethyl methyl carbonate: ethylene carbonate (70:30) with 2% vinyl chloride additive), and lithium metal chips as the counter electrode (Pi-kem, >99%).

Cells underwent two main experiments, formation cycling where cells were run at a constant current of 0.1C for 10 cycles, and rate testing where multiple current rates were employed during charge and discharge in the following order; 0.1, 0.2, 0.5, 1, 5, 1, and 0.1C for 4 cycles each. These

experiments were used to ensure cells showed evidence of typical cell reactions and to assess cell stability at different cycling rates. In both cases, cells were between 1.5 and 0.05 V versus Li^+/Li using a Biologic coin cell cycler with the associated BTlab software.

Supporting Information

Supporting Information is available from the Wiley Online Library or from the author.

Acknowledgements

The authors would like to thank the Faraday Institution (Faraday Institution grant codes FIRG027, project website https://relib.ac.uk/) for funding support. The Royal Academy of Engineering under the Chair in Emerging Technologies program and the Department of Science, Innovation and Technology (DIST) are acknowledged for the financial support of PRS (CiET1718/59).

Conflict of Interest

The authors declare no conflict of interest.

Author Contributions

S.S. and W.D. performed investigation, visualization, wrote, reviewed, and edited the original draft. R. H. performed investigation and visualization. C. L. performed an investigation. P. S. and A.P.A. wrote, reviewed, and edited the final manuscript, performed supervision, and the funding acquisition.

Data Availability Statement

Data is available from the authors on request.

Keywords

direct recycling, lithium-ion batteries, remanufacturing electrode, X-ray micro-computed tomography

Received: August 7, 2024
Revised: January 3, 2025
Published online:

[1] IEA, Global EV Outlook, https://origin.iea.org/reports/global-ev-outlook-2024 (accessed: May 2024).
[2] G. D. J. Harper, E. Kendrick, P. A. Anderson, W. Mrozik, P. Christensen, S. Lambert, D. Greenwood, P. K. Das, M. Ahmeid, Z. Milojevic, W. Du, D. J. L. Brett, P. R. Shearing, A. Rastegarpanah, R. Stolkin, R. Sommerville, A. Zorin, J. L. Durham, A. P. Abbott, D. Thompson, N. D. Browning, B. L. Mehdi, M. Bahri, F. Schanider-Tontini, D. Nicholls, C. Stallmeister, B. Friedrich, M. Sommerfeld, L. L. Driscoll, A. Jarvis, et al., *J. Phys. Energy* **2023**, *5*, 021501.
[3] S. Scott, Z. Islam, J. Allen, T. Yingnakorn, A. Alflakian, J. Hathaway, A. Rastegarpanah, G. D. J. Harper, E. Kendrick, P. A. Anderson, J. Edge, L. Lander, A. P. Abbott, *Next Energy* **2023**, *1*, 100023.
[4] G. Harper, R. Sommerville, E. Kendrick, L. Driscoll, P. Slater, R. Stolkin, A. Walton, P. Christensen, O. Heidrich, S. Lambert, A. Abbott, K. Ryder, L. Gaines, P. Anderson, *Nature* **2019**, *575*, 75.
[5] D. A. Ferreira, L. M. Z. Prados, D. Majuste, M. B. Mansur, *J. Power Sources* **2009**, *187*, 238.
[6] W. Lv, Z. Wang, H. Cao, Y. Sun, Y. Zhang, Z. Sun, *ACS Sustainable Chem. Eng.* **2018**, *6*, 1504.
[7] Z. Sun, H. Cao, Y. Xiao, J. Sietsma, W. Jin, H. Agterhuis, Y. Yang, *ACS Sustainable Chem. Eng.* **2017**, *5*, 21.
[8] V. Halleux, *European Parliament Briefing* **2022**, 1, https://www.europarl.europa.eu/RegData/etudes/ATAG/2022/729285/EPRS_ATA(2022)729285_EN.pdf.
[9] L. Li, F. Dababneh, J. Zhao, *Appl. Energy* **2018**, *226*, 277.
[10] L. Lander, C. Tagnon, V. Nguyen-Tien, E. Kendrick, R. J. R. Elliott, A. P. Abbott, J. S. Edge, G. J. Offer, *Appl. Energy* **2023**, *331*, 120437.
[11] J. Diekmann, C. Hanisch, L. Frobose, G. Schalicke, T. Loellhoeffel, A. S. Folster, A. Kwade, *J. Electrochem. Soc.* **2017**, *164*, 6184.
[12] L. Gaines, Q. Dai, J. T. Vaughey, S. Gillard, *Recycling* **2021**, *6*, 31.
[13] C. Lei, I. Aldous, J. M. Hartley, D. L. Thompson, S. Scott, R. Hanson, P. A. Anderson, E. Kendrick, R. Sommerville, K. S. Ryder, A. P. Abbott, *Green Chem.* **2021**, *23*, 4710.
[14] A. T. Sargent, Z. Henderson, A. S. Walton, B. F. Spencer, L. Sweeney, W. R. Flavell, P. A. Anderson, E. Kendrick, P. R. Slater, P. K. Allan, *J. Mater. Chem. A* **2023**, *11*, 9579.
[15] S. Scott, P. Mukherjee, C. Lei, J. M. Hartley, A. P. Abbott, K. S. Ryder, *J. Power Sources* **2024**, *594*, 233993.
[16] P. J. Withers, C. Bouman, S. Carmignato, V. Cnudde, D. Grimaldi, C. K. Hagen, E. Maire, M. Manley, A. Du Plessis, S. R. Stock, *Nat. Rev. Methods Prim.* **2021**, *1*, 18.
[17] P. Pietsch, V. Wood, *Annu. Rev. Mater. Res.* **2017**, *47*, 451.
[18] T. M. M. Heenan, C. Tan, J. Hack, D. J. L. Brett, P. R. Shearing, *Mater. Today* **2019**, *31*, 69.
[19] J. L. Houx, D. Kramer, *Energy Reports* **2021**, *7*, 9.
[20] X. Lu, A. Bertei, D. P. Finegan, C. Tan, S. R. Daemi, J. S. Weaving, K. B. O'Regan, T. M. M. Heenan, G. Hinds, E. Kendrick, D. J. L. Brett, P. R. Shearing, *3D Nat. Commun.* **2020**, *11*, 2079.
[21] W. Du, Z. Hao, F. Iacoviello, L. Sheng, S. Guan, Z. Zhang, D. J. L. Brett, F. R. Wang, P. R. Shearing, *Small Methods* **2021**, *5*, 2001193.
[22] J. Lin, S. Zhao, T. G. Tranter, Z. Zhang, F. Peng, D. Brett, R. Jervis, P. R. Shearing, *Electrochim. Acta* **2023**, *443*, 141983.
[23] Y. S. Zhang, N. E. Courtier, Z. Zhang, K. Liu, J. J. Bailey, A. M. Boyce, G. Richardson, P. R. Shearing, E. Kendrick, D. J. L. Brett, *Adv. Energy Mater.* **2022**, *12*, 2102233.
[24] A. Fordham, Z. Milojevic, E. Giles, W. Du, R. E. Owen, S. Michalik, P. A. Chater, P. K. Das, P. S. Attidekou, S. M. Lambert, P. K. Allan, P. R. Slater, P. A. Anderson, R. Jervis, P. R. Shearing, D. J. L. Brett, *Joule* **2023**, *7*, 2622.
[25] W. Du, R. E. Owen, A. Jnawali, T. P. Neville, F. Iacoviello, Z. Zhang, S. Liatard, D. J. L. Brett, P. R. Shearing, *J. Power Sources* **2022**, *520*, 230818.
[26] M. M. Kabir, D. E. Demirocak, *Int. J. Energy Res.* **2017**, *41*, 1963.
[27] I. Laresgoiti, S. Käbitz, M. Ecker, D. U. Sauer, *J. Power Sources* **2015**, *300*, 112.
[28] S. S. Zhang, *J. Power Sources* **2006**, *162*, 1379.
[29] M. Yoshio, T. Tsumura, N. Dimov, *J. Power Sources* **2006**, *163*, 215.
[30] S. J. An, J. Li, C. Daniel, D. Mohanty, S. Nagpure, D. L. Wood, *Carbon N. Y.* **2016**, *105*, 52.
[31] D. Burow, K. Sergeeva, S. Calles, K. Schorb, A. Börger, C. Roth, P. Heitjans, *J. Power Sources* **2016**, *307*, 806.

[32] A. Missyul, I. Bolshakov, R. Shpanchenko, *Powder Diffr.* **2017**, *32*, S56.
[33] L. Alcaraz, C. Díaz-Guerra, R. Fernández-Martínez, M. B. Gómez-Mancebo, B. Sotillo, I. Llorente, F. A. López, *Mater. Charact.* **2024**, *209*, 113695.
[34] M. Y. A. Mostafa, A. Mostafa, M. Abdel-Rahman, E. E. Assem, A. Ashour, E. A. Badawi, *Mater. Today Proc.* **2023**, https://doi.org/10.1016/j.materpr.2023.04.252.
[35] A. D. Jara, A. Betemariam, G. Woldetinsae, J. Y. Kim, *Int. J. Min. Sci. Technol.* **2019**, *29*, 671.
[36] T. R. Jow, S. A. Delp, J. L. Allen, J.-P. Jones, M. C. Smart, *J. Electrochem. Soc.* **2018**, *165*, A361.
[37] K. Persson, V. A. Sethuraman, L. J. Hardwick, Y. Hinuma, Y. S. Meng, A. van der Ven, V. Srinivasan, R. Kostecki, G. Ceder, *J. Phys. Chem. Lett.* **2010**, *1*, 1176.
[38] B. Niu, J. Xiao, Z. Xu, *J. Hazard. Mater.* **2022**, *439*, 129678
[39] R. Nölle, K. Beltrop, F. Holtstiege, J. Kasnatscheew, T. Placke, M. Winter, *Mater. Today* **2020**, *32*, 131.
[40] S. J. Cooper, A. Bertei, P. R. Shearing, J. A. Kilner, N. P. Brandon, *SoftwareX* **2016**, *5*, 203.